doi:10.1093/brain/awaa235 BRAIN 2020: 143; 2911–2928 | 2911

BRAIN
A JOURNAL OF NEUROLOGY

YIF1B mutations cause a post-natal neurodevelopmental syndrome associated with Golgi and primary cilium alterations

Jorge Diaz,[1,#] Xavier Gérard,[2,†,*] Michel-Boris Emerit,[1,‡,*] Julie Areias,[1] David Geny,[1,‡] Julie Dégardin,[3] Manuel Simonutti,[3] Marie-Justine Guerquin,[4] Thibault Collin,[5] Cécile Viollet,[1,‡] Jean-Marie Billard,[1,§] Christine Métin,[6] Laurence Hubert,[2] Farzaneh Larti,[7] Kimia Kahrizi,[7] Rebekah Jobling,[8] Emanuele Agolini,[9] Ranad Shaheen,[10,¶] Alban Zigler,[11] Virginie Rouiller-Fabre,[4] Jean-Michel Rozet,[2] Serge Picaud,[3] Antonio Novelli,[9] Seham Alameer,[12] Hossein Najmabadi,[7] Ronald Cohn,[8] Arnold Munnich,[2] Magalie Barth,[11] Licia Lugli,[13] Fowzan S. Alkuraya,[10] Susan Blaser,[14] Maha Gashlan,[10] Claude Besmond,[2] Michèle Darmon[1,6] and Justine Masson[1,6]

*These authors contributed equally to this work.

Human post-natal neurodevelopmental delay is often associated with cerebral alterations that can lead, by themselves or associated with peripheral deficits, to premature death. Here, we report the clinical features of 10 patients from six independent families with mutations in the autosomal *YIF1B* gene encoding a ubiquitous protein involved in anterograde traffic from the endoplasmic reticulum to the cell membrane, and in Golgi apparatus morphology. The patients displayed global developmental delay, motor delay, visual deficits with brain MRI evidence of ventricle enlargement, myelination alterations and cerebellar atrophy. A similar profile was observed in the *Yif1b* knockout (KO) mouse model developed to identify the cellular alterations involved in the clinical defects. In the CNS, mice lacking *Yif1b* displayed neuronal reduction, altered myelination of the motor cortex, cerebellar atrophy, enlargement of the ventricles, and subcellular alterations of endoplasmic reticulum and Golgi apparatus compartments. Remarkably, although YIF1B was not detected in primary cilia, biallelic *YIF1B* mutations caused primary cilia abnormalities in skin fibroblasts from both patients and *Yif1b*-KO mice, and in ciliary architectural components in the *Yif1b*-KO brain. Consequently, our findings identify *YIF1B* as an essential gene in early post-natal development in human, and provide a new genetic target that should be tested in patients developing a neurodevelopmental delay during the first year of life. Thus, our work is the first description of a functional deficit linking Golgipathies and ciliopathies, diseases so far associated exclusively to mutations in genes coding for proteins expressed within the primary cilium or related ultrastructures. We therefore propose that these pathologies should be considered as belonging to a larger class of neurodevelopmental diseases depending on proteins involved in the trafficking of proteins towards specific cell membrane compartments.

1 INSERM UMR894, Center for Psychiatry and Neuroscience, Paris F-75014, Université Paris Descartes, Sorbonne Paris Cité – Paris 5, France
2 INSERM UMR-S1163 Imagine Institute for Genetic Diseases, Paris Descartes-Sorbonne Paris Cité University, France
3 INSERM UMR-S968, Institut de la vision, Centre Hospitalier National d'Ophtalmologie des Quinze-Vingts, Paris F-75012, Université Pierre et Marie Curie, France
4 CEA, DSV, IRCM, SCSR, Fontenay-Aux-Roses, France
5 Saint Pères Paris Institute for the Neurosciences CNRS - UMR 8003 Université de Paris, Paris 75006, France
6 INSERM, UMR-S1270, Institut du Fer à Moulin, Sorbonne Université, Paris F-75005, France

Received January 24, 2020. Revised May 29, 2020. Accepted June 13, 2020

7 University of Social Welfare and Rehabilitation Sciences, Genetics Research Center, Tehran 19834, Iran
8 The Hospital for Sick Children, Molecular Genetics, Toronto, Canada
9 Laboratory of Medical Genetics, Bambino Gesù Children's Hospital, 00146 Rome, Italy
10 King Faisal Specialist Hospital and Research Center, Developmental Genetics Unit, Riyadh 11211, Saudi Arabia
11 CHU Angers, Génétique, France
12 Department of Pediatrics, King Khaled National Guard Hospital, King Abdulaziz Medical City, Jeddah, Saudi Arabia
13 Division of Neonatal Intensive Care Unit, Department of Pediatrics, University Hospital, 41125 Modena, Italy
14 Division of Neuroradiology, The Hospital for Sick Children, University of Toronto, Toronto, Canada

[#]Present address: Université de Paris, CNRS, Integrative Neuroscience and Cognition Center, F-75006 Paris, France
[†]Present address: Unit of Retinal Degeneration and Regeneration, Service, d'Ophtalmologie de l'Université de Lausanne, Hôpital Ophtalmique Jules-Gonin - Fondation Asile des aveugles, CH-1002 Lausanne, Switzerland
[‡]Present address: Institute of Psychiatry and Neuroscience of Paris, INSERM U1266, Université de Paris, France
[§]Present address: Normandie Univ, UNICAEN, INSERM, GIP CYCERON, COMETE, Caen, France
[¶]Present address: Qatar Biomedical Research Institute (QBRI), Doha, Qatar

Correspondence to: Justine Masson
INSERM, UMR-S1270, Institut du Fer à Moulin
17 Rue du Fer à Moulin, 75005 Paris, France
E-mail: justine.masson@inserm.fr

Keywords: neurodevelopmental delay; ER; Golgi; primary cilium
Abbreviation: ER = endoplasmic reticulum

Introduction

The main causes of infant mortality during the first year of life are foetal encephalopathy, seizures or brain alterations that develop after birth. Genetic studies have demonstrated that single gene defects are often responsible for these alterations. Among mutations that have been shown to impair neurodevelopmental processes, those affecting Golgi apparatus trafficking genes do not cause anomalies at birth, but alterations appear during early post-natal development (Passemard *et al.*, 2017). Trafficking proteins are involved in multiple secretory pathways requiring a complex ballet of vesicular carriers organizing sorting, packing, routing and recycling through interactions with Rab GTPases, Rab effectors or Rab regulators. Mutations in genes coding for trafficking proteins have been shown to cause severe neurodevelopmental delay, white matter defects and intellectual disability in human (Mir *et al.*, 2009; Seifert *et al.*, 2011; Handley *et al.*, 2013; Liegel *et al.*, 2013; Feinstein *et al.*, 2014; Shamseldin *et al.*, 2016). We previously characterized, in rodent, YIF1B, a trafficking protein orthologue of YIF1P that was initially identified in *Saccharomyces cerevisiae* as interacting with YIP1P (a Golgi apparatus membrane protein able to bind Ras-like GTPases) and essential for secretion (Matern *et al.*, 2000). YIF1B is localized in the intermediate compartment between the endoplasmic reticulum (ER) and the Golgi apparatus. It participates in the anterograde traffic from the ER to the cell membrane of the membrane-bound vesicular stomatitis virus G protein in HeLa cells and in neurons. Its deletion in mouse neurons leads to Golgi apparatus disorganization (Alterio *et al.*, 2015) and alteration of the dendritic targeting of a specific serotonergic receptor (Carrel *et al.*, 2008). A recent study identified mutations in the *YIF1B* gene in patients displaying progressive encephalopathy with various degrees of mixed movement disorder, microcephaly and epilepsy (AlMuhaizea *et al.*, 2020). In the current study, we also identified mutations of the *YIF1B* gene in six families comprising 10 affected patients with neurological deficits that could not be classified by clinicians as a specific pathology, but whose clinical manifestations were close to those observed in Golgipathies. We took advantage of the *Yif1b*-KO mouse model to investigate the cellular, subcellular and physiological alterations that could underlie clinical features in patients carrying *YIF1B* mutations. Our investigations demonstrate that *Yif1b* depletion in mice induces central nervous system alterations similar to those observed in patients. Moreover, investigating cellular and subcellular structural integrity in the *Yif1b*-KO mouse model allowed us to infer that some of the clinical features observed in patients could be attributed to neuronal degeneration associated with Golgi apparatus, ER and primary cilium alterations.

Materials and methods

Human subjects

Clinical and molecular data from 10 patients with *YIF1B* variants from different clinical centers in France, Saudi Arabia, Iran, Canada and Italy were collected through clinical or genetics network such as GeneMatcher (Sobreira *et al.*, 2015). None of these patients were previously reported. Each referring clinician filled out a table with detailed birth parameters,

developmental, neurological, behavioural and seizure medical history including EEG, EMG and imaging data when available.

DNA of all members of Families 1–6 was studied by whole-exome analysis. Informed consent was obtained from each patient included in this study and this study protocol conformed to the ethical guidelines of the 1975 Declaration of Helsinki as reflected in *a priori* approval by the Institution's human research committee (Comité de Protection des Personnes, Ile de France II, Approval ≠ 2015-03-03/DC 2014–2272, Paris, France).

Cell culture

Human and murine primary fibroblasts were successfully derived from skin biopsies and cell lines were isolated by selective trypsinization and proliferated at 37°C, 5% CO_2 in Opti-MEM™ GlutaMAX™ I medium (Invitrogen) supplemented with 10% foetal bovine serum (FBS, Invitrogen), 1% Ultroser™ G substitute serum (Pall), and 1% streptomycin/penicillin (Invitrogen). Fibroblasts between passages seven and nine were plated at 10^5 cells/well in 24-well plates. Patient lymphoblastic cell lines were grown in RPMI medium, 10% FBS, sodium pyruvate and penicillin/streptomycin.

Animals

Homozygous *Yif1b*-KO mice and control littermates were obtained from previously established colonies (Alterio *et al.*, 2015). Experimental mice were housed with companions of the same gender and breeding mice in 'trio' (two females with one male) in standard cages type L2 with Celle Bel MAXI-25 cellulose bedding and maintained under a 12-h light/dark cycle with constant temperature (23.0 ± 1.0°C) and humidity (60%), with food and water *ad libitum*. Experiments were performed during the light phase on 3–5- and 12-month-old male mice, and compared to matched controls. All efforts were made to reduce the number of animals used in experiments. Experiments were performed in agreement with the institutional guidelines for use of animals and their care, in compliance with national and international laws and policies (Council directives no. 87–848, October 19, 1987, Ministère de l'Agriculture et de la Forêt, Service Vétérinaire de la Santé et de la Protection Animale, permissions no. 75-805 to J.M.). All protocols were approved by the ethical committee #C2EEA34 and were licensed by the Directorate General for Research and Innovation (French MESR) under protocol authorization #00717.06. Experimental design was carried out according to ARRIVE guidelines.

Antibodies

The following primary antibodies were used: mouse monoclonal anti-Arl13B antibody (Antibodies Inc, 1/500); anti-CTR433 antibody (1/1600) (Jasmin *et al.*, 1989), anti-γ-tubulin antibody (Sigma, 1/20 000); rabbit polyclonal anti-acetylated tubulin antibody (Sigma, 1/2000), anti-Calbindin D28K antibody (Sigma, 1/3000), anti-Iba1 antibody (Wako, 1/800), anti-pericentrin antibody (Abcam, 1/1000), anti-CEP83 (Sigma, 1/500), anti-CEP164 antibody (Sigma, 1/1000), anti-Myelin Basic Protein (1/200; Colman *et al.*, 1982); goat polyclonal anti-rootletin antibody (Santa-Cruz, 1/500). Fluorophore-labelled secondary donkey antibodies used were Cy3-conjugated anti-rabbit antibody, Alexa 488-conjugated anti-goat antibody, Cy3-conjugated anti-mouse antibody (Jackson ImmunoResearch, 1/500).

Western blot analyses

Cultured fibroblasts were harvested and homogenized by sonication in sample buffer (Laemmli, 1970). Proteins (2 µg), quantified using the Pierce BCA Reducing Agent kit, were analysed by SDS-PAGE and blotted to polyvinylidene difluoride (PVDF) membrane. Incubation with affinity-purified rabbit anti-YIF1B antiserum (1/1000) (Carrel *et al.*, 2008) and mouse anti-actin monoclonal antibody (Sigma, 1/5000) was performed. Immunoreactivity was detected using a chemo-luminescence detection kit and a ChemiDoc Touch Imaging System (Bio-Rad).

Histochemical and immunostaining methods and quantitative analysis of labelling

Mice were deeply anaesthetized using pentobarbital (60 mg/kg,) and perfused by trans-cardiac puncture with 0.9% NaCl (warmed at 37°C, 10 ml) followed by paraformaldehyde (4%, ice-cooled, 150 ml). Brains were removed, post-fixed at 4°C for 1 h and rinsed in phosphate buffer 0.1 M. Free floating sections (40 µm) were obtained using a Leica vibratome VT1000E and frozen sections using a Leica cryostat CM3000.

Luxol fast blue/Cresyl violet staining

Vibratome sections and frozen sections were incubated at 53°C overnight in Luxol fast blue 0.1%. Sections were rinsed in distilled water before differentiation in lithium carbonate solution 0.05% for 30 s. Slides were rinsed in distilled water and counterstained at 53°C for 1 h in Cresyl violet 0.1%. Sections were dehydrated, cleared and mounted in a resinous medium.

Immunofluorescence on sections

Floating sections were blocked for 1 h at room temperature with TBS, Tween-20 0.1% (T20) containing 5% normal donkey (v/v), 0.4% BSA (w/v) and 0.1% gelatin (w/v) before incubation overnight at 4°C with primary antibodies diluted in TBS-T20 containing 0.4% BSA and 0.1% gelatin. After primary antibody incubations, the sections were washed three times (10 min each) in TBS–T20 containing 0.1% gelatin and then incubated for 1 h at room temperature with complementary fluorophore-labelled secondary donkey antibodies. After PBS washes, sections were mounted in Fluoromount-G™ solution (CliniSciences). Immunofluorescence images were generated using a Leica TCS SP5 microscope (PL-APO 63×, NA1.4 oil, Imaging medium Leica).

Immunofluorescence on cells

Cultured fibroblasts were grown to 80% confluency and serum-starved for 48 h. Cells were fixed with 100% methanol and processed for immunofluorescent staining as previously described (Alterio *et al.*, 2015). Coloured and fluorescence images were generated using a Zeiss photomicroscope (25× magnification, bright field illumination) and a Zeiss LSM700 confocal microscope respectively (×40 magnification, Carl Zeiss) or a Leica TCS SP5, PL APO microscope (×63 and ×100).

Two- and three-dimensional analysis of labelling

ImageJ (2D analysis) and Volocity software (3D analysis) were used for image processing and quantification. Quantification of the fluorescent myelin basic protein (MBP) immunostaining intensity was performed using ImageJ software. The ciliary length was quantified by maximal axis using Arl13B and acetylated tubulin labelling close to basal bodies labelled by g-tubulin and pericentrin respectively using the Volocity software.

Electron microscopy

For electron microscopy section, perfusion was performed using 2.5% glutaraldehyde and 2% paraformaldehyde. Brain and testis were removed and post-fixed in the same fixative at 4°C for 4 h and rinsed in phosphate buffer 0.1 M. Vibratome free floating coronal or sagittal sections taken throughout the cerebellum (150-µm thick), the hippocampus and the testis (200-µm thick) were maintained at 4°C in phosphate buffer saline 50 mM, pH 7.4. Tissue pieces of 2 mm × 1 mm from both cerebellar lobules 9 and 10, from the hippocampal CA1 region and from the seminiferous tubules were dissected and post-fixed for 30 min in 1% osmium tetroxide, rinsed and incubated 1 h in a solution of 1% uranyl acetate in water. After dehydration in a graded series of ethanol solutions, pieces of seminiferous tubules were flat-embedded in epoxy resin (Epon) and allowed to polymerize for 48 h at 60°C. The ultrathin sections, cut with a Reichert ultramicrotome, were mounted on mesh grids, stained with lead citrate and analysed on a JEOL 100 electron microscope equipped with a GATAN CCD camera.

Behaviour

Spontaneous locomotion

Locomotor activity was measured using an actimeter, a computer-based photo-beam apparatus (Actisystem II, Panlab). Actimeter boxes (area: 30 × 15 cm; height: 18 cm; with grid floor) detected mouse movements by means of infrared light beams. Mice were placed in the boxes for 60 min and horizontal activity was monitored (in centimetres).

Motor coordination

In the Locotronic apparatus (Intellibio Innovation), the mice crossed a 124 × 28 × 20 cm flat ladder with bars (7 mm in diameter) set 1 cm apart. Infrared sensors situated above and below the bars monitored paw errors. Mice were habituated to learn to cross the ladder and then placed in the apparatus in three conditions, a first session with no traps, a second with traps (five withdrawing bars separated from five to seven bars) and a third with no traps. During these tests, errors of hind legs were counted. For basal and learned motor coordination, each mouse was placed onto the horizontal rod of an accelerating Rotarod apparatus (model 7650, Ugo-Basile), rotating at a speed increasing from 4 to 40 rpm over 5 min. The time required for the mouse to fall from the rod was recorded. Mice were acclimatized to the apparatus by placing them for 2 min on the rod at 5 rpm, 3 min before the first test. Motor coordination performance was evaluated the first day just after acclimatization session of each mouse (with a 20-min resting period between two successive training). Mice were trained three times a day on the two consecutive days. Motor coordination performance of each mouse was determined by the longer time to fall on the three trials.

Visual performances: optomotor response

Mice were placed on a platform in the form of a grid (11.5 cm diameter, 19.0 cm above the bottom of the drum) surrounded by a motorized drum (29.0 cm diameter) that could be revolved clockwise or anti-clockwise at two revolutions per min, the optimal velocity for evoking an optokinetic response in the mouse. After 10 min of adaptation in the dark, vertical black and white stripes of a defined spatial frequency were presented to the animal. These stripes were rotated alternately clockwise and anti-clockwise, for 2 min in each direction with an interval of 30 s between the two rotations. Various spatial frequencies subtending 0.06, 0.13, 0.25 and 0.5 cycles/degree were tested individually on different days in a random sequence. Animals were videotaped with a digital video camera (Sony, DCR-TRV24E) for subsequent scoring of head tracking movements. Tests were performed in scotopic conditions, using the night shot position of the camera. Head movements were scored only if the angular speed of the head corresponded to that of the drum rotation.

Retinal electrophysiology

Electroretinograms (ERG) were performed in male adult mice, dark-adapted for 12 h prior to recording. They were anaesthetized by intra-peritoneal injection of ketamine/xylazine (10%/7.5%, diluted in 0.9% NaCl, 10 µl/g body weight). Corneas were anaesthetized with oxybuprocaine hydrochloride (0.4%, Thea Lab) and pupils were dilated with tropicamide (0.5%, Thea Lab). Each animal was placed on a heating pad, eyelids were retracted to maintain eyes open during recording. A gold electrode was placed onto corneas with a drop of methylcellulose (Ocry-gel) while the neutral and reference electrodes were placed on the tail and head of animals, respectively. Light stimulations were delivered in a Ganzfeld with flash intensity of 0.04–8 cds/m^2 for scotopic and 8 cds/m^2 for photopic conditions. The flicker ERG was also used to isolate cone responses at 10-Hz flash frequencies and 1 cds/m^2 intensity. Amplitudes of the scotopic a- and b-waves were measured at the maximum negative and positive peaks of the recordings with respect to the baseline before stimulation.

Statistical analysis

Statistical software used to perform analyses was Prism Graph Pad. The significance of the data obtained was determined by performing unpaired Student's *t*-test, Mann-Whitney test, Wilcoxon test, two-way ANOVA followed by *post hoc* tests. *P*-values were considered significant when $\leqslant 0.05$: $^{****}P \leqslant 0.0001$, $^{***}P \leqslant 0.001$, $^{**}P \leqslant 0.01$, $^{*}P \leqslant 0.05$.

Data availability

The data that support the findings of this study are available from the corresponding author, upon reasonable request.

Results

Identification of mutations in the *YIF1B* gene in patients displaying neurodevelopmental delay

In 10 patients displaying severe neurodevelopmental delay, from six unrelated families, we have identified by whole exome sequencing, biallelic homozygous mutations (Families 1–4, Patients 1.1, 1.2, 2.1, 2.2, 3.1, 3.2, 4.1 and 4.2) and two compound heterozygous mutations (Families 5 and 6, Patients 5.1 and 6.1) in the *YIF1B* gene (Fig. 1A, Supplementary Table 1 and Supplementary Fig. 1).

In the two affected sibs of Family 1 (born from Somalian parents from the same tribe), the homozygous mutation leads to a stop codon at the glutamate residue in position 200 (p.Glu200*), resulting in a short truncated protein with only one transmembrane domain (Fig. 1B and Supplementary Fig. 1). In Family 2, affected children (born from French parents from the same village with probable distant consanguinity) carried a homozygous variation in the splice donor site of intron 5. The splicing effects of this variant was identified by sequencing the *YIF1B* cDNA transcript in immortalized lymphocytes from this patient. The homozygous variation in the splice donor site of intron 5 produced a skipping of exon 5, which leads to a frameshift followed by a premature stop codon 17 amino acids downstream (p.Ala161Glyfs*18). Patients from Family 3 (born from Saudi parents from the same tribe) carried a single homozygous nucleotide duplication producing a frameshift leading to a truncated protein 12 amino acids downstream (p.Ala60Cysfs*13) that lacks all transmembrane domains. In Family 4, the two affected sibs (born from Iranian parents, consanguineous) carried a homozygous variant in the cytosolic N-terminus of YIF1B (p.Lys123Gln). In the two other families, Patients 5.1 and 6.1 carried two different variants inherited from each parent. The affected child, Patient 5.1 carried one variant identical to Patient 2.1 (skipping of exon 5 confirmed also on DNA sequencing from grown immortalized lymphocytes; Supplementary Fig. 1) and a frameshift (p.Met233Serfs*6) leading to a truncated protein lacking the three last transmembrane domains. The affected child, Patient 6.1, carried a premature stop codon (p.Tyr167*) on one allele, leading to a short truncated protein with only one transmembrane domain, and a frameshift leading to a truncated protein 35 amino acids downstream (p.Ala193Profs*36) on the other one (Fig. 1B and Supplementary Fig. 1).

YIF1B splice-site and point mutations identified in patients behave as loss of function alleles

We investigated the expression level of the YIF1B protein in cells isolated from patients. Western blot experiments were performed with a YIF1B antibody directed against the N-terminal cytoplasmic peptide of YIF1B, which recognizes all YIF1B variant proteins mutated and/or truncated downstream of the antigenic site (Carrel *et al.*, 2008). In immortalized lymphocytes from Patients 2.1, and 5.1, no YIF1B protein (full length or truncated, expected at 22 kDa was detected, whereas bands were obtained for control cells at the expected size (34 kDa) (Fig. 1C). We also confirmed the lack of detection of YIF1B protein in fibroblasts cultured from the skin of Patient 2.1 (Fig. 1D). In fibroblasts from Patient 4.2, who carries a missense point mutation (Lys123Gln; Supplementary Fig. 1), only small amounts of YIF1B were detected compared to the control (Fig. 1D).

In conclusion, truncated YIF1B proteins lacking all transmembrane domains were not expressed in cells isolated from these patients and a missense mutation in the third transmembrane domain of the protein was enough to induce a strong decrease of its expression. These observations are similar to those we made on the stability of truncated rat YIF1B proteins. The constructs lacking all the transmembrane domains could not be expressed in COS cells. Moreover, increasing the number of transmembrane domains also increased the level of expression of the *Yif1b* constructs (Al Awabdh *et al.*, 2012).

YIF1B mutations in human cause a new post-natal developmental deficit syndrome

The detailed description of the clinical features of patients is presented in Supplementary Table 1 and a summary of the most common clinical features in Supplementary Table 2. All patient birth parameters are normal, including head circumference. All subjects display developmental deficit starting after birth. Patients with truncated proteins (from Families 1–3, 5 and 6) never achieved or subsequently lost head control and were never able to sit, stand and walk. Patients with point mutations (Patients 4.1 and 4.2) displayed strong physical developmental delay. In all patients, severe cognitive impairment was observed and mental disability was evaluated in patients with point mutations. Motor alterations, such as spasticity, hypotonia and hypertonia were observed in all patients. Other neurological alterations were detected in patients including seizures, swallowing difficulties, dystonia and central hypoventilation. Among patients with *YIF1B* mutations leading presumably to the lack of YIF1B protein, some died prematurely (patients from Families 1 and 2) and some survived under mechanical ventilation and with an effective treatment for their seizures (Patients 5.1 and 6.1). Patients with truncated YIF1B protein who lived with normal respiratory function did not have seizures or pharmaco-resistant seizures (Patients 3.1 and 3.2).

Patients with truncated YIF1B protein had cerebral palsy and abnormalities in their brain structures as detected by brain MRI (Fig. 1E), except for patients from Family 3.

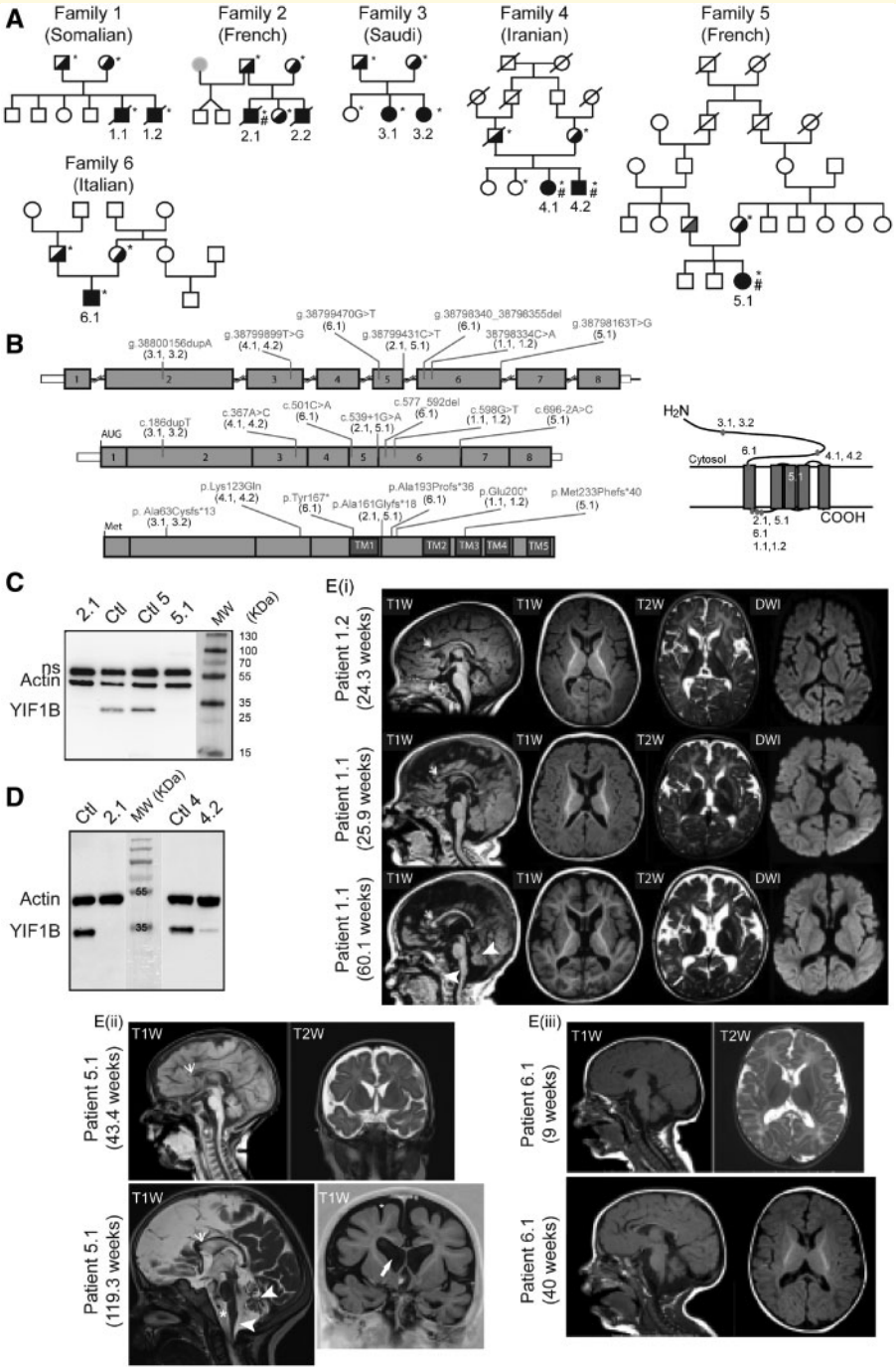

Figure 1 *YIF1B* mutations in six independent families. (**A**) Pedigrees of six families of patients (grey circle was a donor egg). (**B**) Schematic representation of the human *YIF1B* gene, mRNA and protein with five transmembrane domains (TM1–5) and location of the mutations in red (with patient identification) on flat and secondary structure drawing. (**C**) Western blot analysis of YIF1B protein in lymphocytes from Patients 2.1 and 5.1, and control subjects (Ctl, Ctl 5). (**D**) Western blot analysis of the YIF1B protein in fibroblasts isolated from skin biopsies of Patients 2.1 and 4.2 and control subjects (Ctl, Ctl 4). ns = non-specific. (**E**) MRI from the patients. [**E(i)**] Patients from family one with sagittal T_1-weighted (T1W), axial T_1-weighted and T_2-weighted (T2W) images (DWI images show there is no diffusion restriction). Images were taken at 24.3 weeks for Patients 1.2 and at 25.9, and 60.1 weeks for Patient 1.1, who survived longer. [**E(ii)**] Patient 5.1 with sagittal T_1-weighted and axial T_2-weighted at 43.3 and 119.3 weeks. [**E(iii)**] Patient 6.1 with sagittal and axial T_1-weighted images at 9 and 40 weeks. Note thin corpus callosum, small cerebellum and abnormal pons (small white arrows on T_1-weighted images), enlargement of the ventricle (white arrow on T_1-weighted image at 119.3 weeks), reduction of white matter, and volume loss with enlargement of the lateral and third ventricles and prominence of the pericerebral fluid spaces and of the Sylvian fissures.

MRIs were obtained from four patients (Patients 1.1, 1.2, 5.1 and 6.1) at two developmental stages (except for Patient 1.2 that died early). Patients showed delayed myelination and/or thin corpus callosum the first year of life (Fig. 1E, white arrows on parasagittal T_1 images). Progressive cerebellar vermian and pons atrophies (Fig. 1E, white arrowheads), and increase of the cisterna magna size are observed [Fig. 1E(ii), white star]. Progressive parenchymal loss and a ventricular dilatation are detectable in all patients. The strongest phenotype is observed in Patient 5.1 who was older than the other patients at the time of the last MRI [Fig. 1E(ii)]. Comparison of two MRI from the same patient (Patient 6.1) at the age of 9 and 40 weeks suggests that defects appeared after birth as no alteration was detected at 9 weeks [Fig. 1E(iii)].

To understand the requirement for YIF1B at the cell, tissue and organism levels, we characterized the mice constitutively lacking the *Yif1b* gene (*Yif1b*-KO) (Alterio *et al.*, 2015).

Yif1b-KO mice have deficits similar to those observed in patients carrying YIF1B mutations

Yif1b-KO mice did not present post-natal lethality. Therefore, we investigated phenotypes in these mutant mice that were related to clinical traits of patients that could be responsible for premature death in human such as hypoventilation and seizures (Supplementary material). Ventilation in adult *Yif1b*-KO mice was evaluated using plethysmography under normal air and in hypercapnia. We demonstrated that *Yif1b* deletion has no impact on the ventilation of mice (Supplementary Fig. 2A). Patients show seizures beginning as early as 4 months of age, but adult *Yif1b*-KO mice did not display spontaneous seizures. We then tested the sensitivity of the mutants in pharmacological induced kindling conditions and demonstrated that neither the latencies to present myoclonic-clonic or generalized seizures were decreased in *Yif1b*-KO after acute injection of pentylenetetrazole (Supplementary Fig. 2B).

In mice, YIF1B did not seem to be essential for ventilation or in the equilibrium of excitatory/inhibitory balance in the cortex and the hippocampus, a function known to be altered in epilepsy, which suggests that some compensatory mechanism occurred in this species. We then investigated other phenotypic alterations in the *Yif1b*-KO adult mice that could model the defects observed in patients.

Patients carrying *YIF1B* mutations exhibit visual impairment (nystagmus, strabismus, optic atrophy and retinopathy, Supplementary Table 1). In Patients 3.1 and 5.1, lack of visual evoked potential was observed even with flash stimulation suggesting retinal dysfunction. Likewise, the patient from Family 5 of the recently published study on patients carrying *YIF1B* mutations also exhibited cortical blindness (AlMuhaizea *et al.*, 2020). Hence, we further explored visual functions in the *Yif1b*-KO mice. Mutant mice showed head movements demonstrating some visual perception but without the frequency-dependent increase observed in wild-type mice (Fig. 2A). *Yif1b*-KO mice displayed visual performance deficits in optometer response. We then investigated retinal physiology in *Yif1b*-KO mice and showed that the visual impairment was caused by retinal dysfunction, as indicated by the electroretinogram amplitude decreases (Fig. 2B and C). In scotopic condition, if the a-wave reduction and latency increase indicated an impaired phototransduction in photoreceptors [Fig. 2C(i)], the further b-wave amplitude decrease [Fig. 2C(ii)] was consistent with the optic nerve atrophy in patients.

Since patients display several motor and locomotor deficits (Supplementary Tables 1 and 2), we explored these functions in *Yif1b*-KO mice. Basal locomotion was normal in *Yif1b*-KO mice (Fig. 3A); however, when fine locomotor coordination was explored by the locotronic test, a deficit in *Yif1b*-KO mice was observed with an increase of mistakes on the horizontal ladder (Fig. 3B). Motor coordination behaviour was assessed using the Rotarod test. Performances on the first day of Rotarod testing in *Yif1b*-KO were normal compared to wild-type (wild-type = 85.86 ± 8.552 s, $n = 14$; *Yif1b*-KO = 91.25 ± 9.022, $n = 12$; Student's *t*-test, $P > 0.05$); however, coordination learning was altered in *Yif1b*-KO mice performing three consecutive days (Fig. 3C).

Yif1b-KO mice have anatomical cerebral defects similar to those observed in patients

As MRIs from patients revealed specific brain alterations (Supplementary Tables 1 and 2), we investigated the presence of similar defects in the adult brain *Yif1b*-KO mice.

Myelination was evaluated by the level of expression of MBP, which is localized in the myelin sheath surrounding myelinated axons. We focused on motor cortex of *Yif1b*-KO as these mice displayed motor behavioural alterations (Fig. 3) and demonstrated that MBP was reduced in layers I and V–VI (Fig. 4A) consistent with delayed myelination observed in patients (Fig. 1E). Anatomical analyses revealed that *Yif1b* depletion in mice showed a moderate dilatation of the ventricles [Fig. 4B(i and ii)] as observed in patients (Fig. 1E). Finally, in *Yif1b*-KO, cerebellar atrophy was systematically observed [Fig. 4C(i)] as detected in patient brains (Fig. 1E). In mice, this defect was associated with changes in the shape of the cerebellum [Fig. 4C(ii)] and the decrease of cerebellar weight (without brain hypoplasia) [Fig. 4C(iii)].

Cellular and subcellular defects underlying cerebellar atrophy in the *Yif1b*-KO brain

We investigated cellular changes that underlie cerebellar atrophy in the cerebellum of the *Yif1b*-KO mouse. A reduction of 17% of Purkinje cells (identified with calbindin-immunofluorescent labelling) and the disorganization of the dendritic tree of remaining cells were observed, possibly accounting

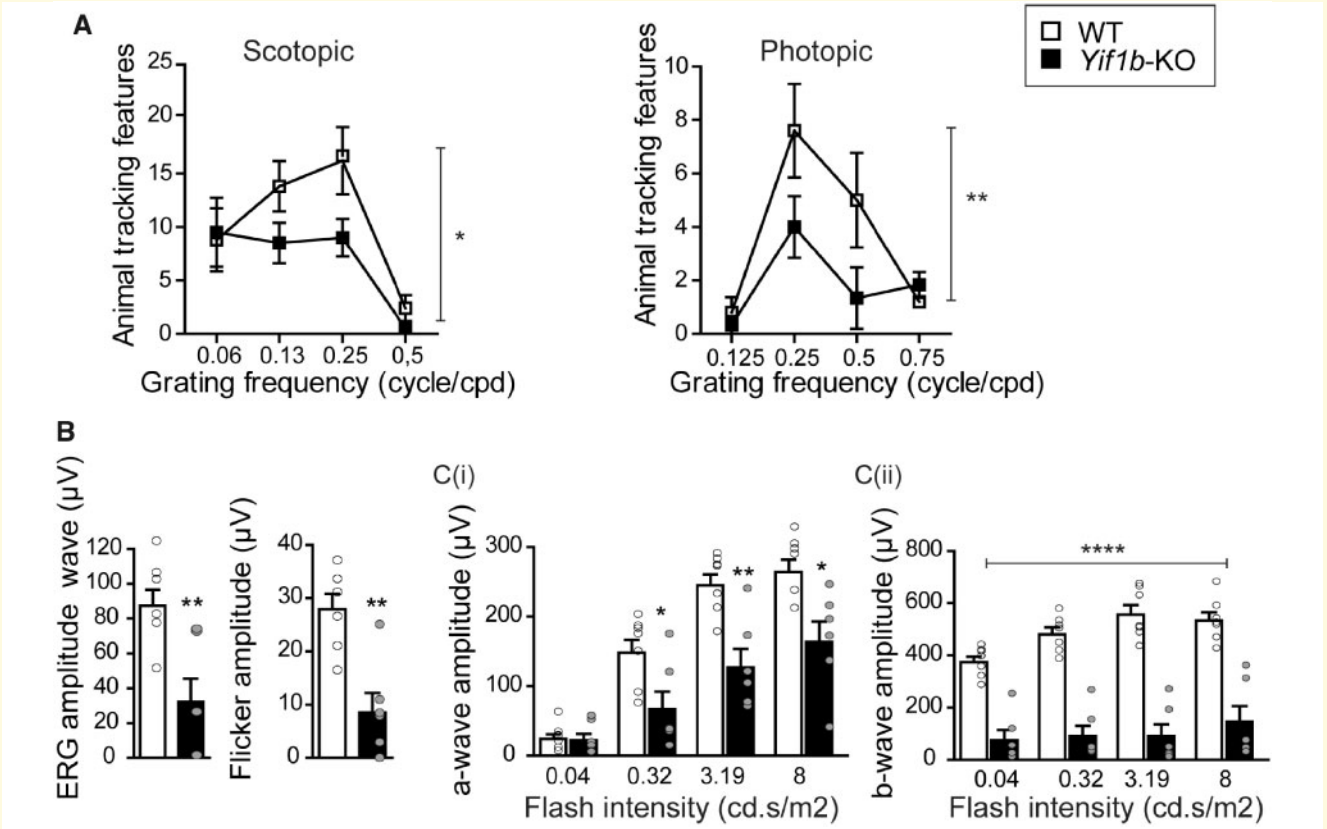

Figure 2 *Yif1b*-KO mice have visual deficits. (**A**) Optometric tests [wild-type (WT), $n = 5$; mutant, $n = 6$]. In scotopic conditions, two-way ANOVA indicated significant differences among spatial frequencies [$F(3,27) = 9.468$; $P < 0.0001$] and genotypes [$F(1,27) = 4.507$; $P = 0.0407$] with no significant optometric stripe × genotype interaction [$F(3,27) = 1.188$, $P = 0.3279$]. In photopic conditions, two-way ANOVA indicated significant differences among spatial frequency [$F(3,27) = 9.367$; $P = 0.001$] and genotypes [$F(1,27) = 5.617$, $P = 0.0233$] and no optometric stripe × genotype interaction [$F(3,27) = 2.142$, $P = 0.1199$]. (**B** and **C**) Abnormal retinal activity of *Yif1b*-KO mice in photopic (**B**) and scotopic (**C**) conditions revealed by electroretinograms recording (wild-type, $n = 7$; *Yif1b*-KO $n = 6$). (**B**) In photopic conditions, electroretinogram amplitude wave and flicker amplitude were significantly reduced in mice *Yif1b*-KO (Student's *t*-test, $P = 0.0049$ for wave amplitude and $P = 0.013$ for flickers). [**C**(**i** and **ii**)]. In scotopic conditions, two-way ANOVA for a-wave indicated significant genotype × flash intensity interaction [$F(3,44) = 3.39$, $P = 0.262$] with a significant difference between genotype at flash intensities > 0.04 cd.s/m^2 [**C**(**i**)] indicating with latency increase an impaired phototransduction in photoreceptors. Two-way ANOVA for b-wave indicated significant difference between genotypes [$F(1,44) = 0.0187$, $P < 0.0001$) and flash intensities [$F(3,44) = 0.0187$] with no genotype × flash intensity interaction [$F(3,44) = 1.625$, $P = 0.1971$] [**C**(**ii**)]. Data are presented as mean ± SEM and data-points are shown. *$P < 0.05$; **$P < 0.01$; ****$P < 0.0001$.

for the decreased molecular layer thickness (Fig. 5A, high magnification images). Interestingly, the decrease of Purkinje cells in mutant mice was not statistically increased between 3 and 12 months of age [Fig. 5A(ii)]. Purkinje cells death was not due to apoptosis, as the number of apoptotic Purkinje cells, detected by TUNEL staining showed no difference between the cerebellum of wild-type and *Yif1b*-KO mice (Supplementary Fig. 6). This indicates that necrotic mechanisms were responsible of the Purkinje cell degeneration as further verified in our ultrastructural study. Purkinje cell degeneration in 3-month-old *Yif1b*-KO mice was confirmed on semithin toluidine blue-stained cerebellum sections in which moderately electron dense Purkinje cell bodies and dendrites were observed (Fig. 5B). As cerebellar glial cells and especially the microglia are sensitive to homeostatic microenvironmental disruptions during disease and neuronal degeneration (Cvetanovic *et al.*, 2015; Tay *et al.*, 2017), we performed Iba1 immunofluorescence to assess the microglial response in the cerebellum. We found not only an increase in the density of microglia cells in the cerebellar cortex of *Yif1b*-KO mice compared to their wild-type littermates [Fig. 5C(i and ii)] but also the presence of hypertrophic microglia in the Purkinje cells and molecular layers, where they were sometimes grouped into foci [Fig. 5C(i)], probably removing debris from degenerating Purkinje cells. Although these microglial responses are generally good indications of their reactive function, further work is needed to assess their cytokine profiles and their interactions with surrounding cells to determine their exact roles in this degenerative process.

We then performed transmission electron microscopy analysis in Purkinje cells layer in wild-type and *Yif1b*-KO mice.

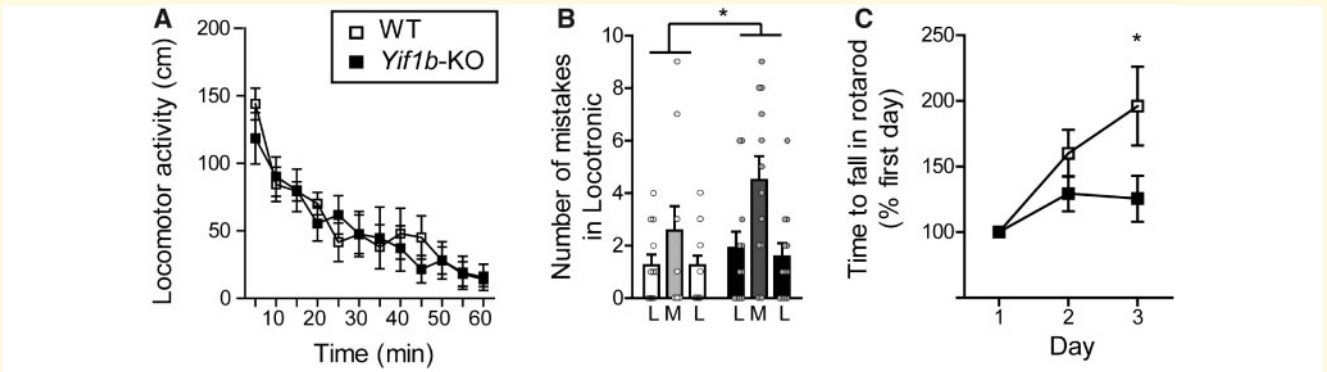

Figure 3 Locomotor and motor functions in *Yif1b*-KO mice. (**A**) Normal basal locomotion of *Yif1b*-KO mice was observed compared to control littermates. Time course of basal locomotor activity was assessed by total photobeam breaks measured in 5-min intervals [wild-type (WT), $n = 7$; *Yif1b*-KO, $n = 5$]. (**B**) Locotronic test revealed an alteration of fine motor coordination in *Yif1b*-KO ($n = 12$) compared to wild-type ($n = 12$). Two-way ANOVA indicated significant difference among sessions (L = test with regular ladder; M = missing bars in the ladder] [$F(2,44) = 5.463$; $P = 0.0076$] and genotypes [$F(1,22) = 4.78$, $P = 0.0397$] with no significant session × genotype interaction [$F(2,44) = 0.6814$, $P = 0.5112$]. (**C**) Alteration in learning ability evaluated by the Rotarod test (wild-type, $n = 14$; *Yif1b*-KO, $n = 13$). No difference was observed at Day 1 (wild-type = 85.86 ± 8.552 s and *Yif1b*-KO = 93.92 ± 8.719 s; Student's *t*-test, $P = 0.5153$). At Day 3, two-way ANOVA indicated a significant effect of time × genotype interaction [$F(2,50) = 3.594$, $P = 0.0348$]. Bonferroni's *post hoc* test showed a significant impact of the mutation. Data are presented as mean ± SEM and data-points are shown. *$P < 0.05$.

Ultrastructural examination of wild-type mice sections (Fig. 6A, C and E) were comparable to those previously described (Palay and Chan-Palay, 1974). In sections from *Yif1b*-KO mice, evident signs of alterations encompassing the cell somata and the entire dendritic arbor were observed, such as an increase of the electron density of the cytoplasm (Fig. 6B) and in the number of lysosome-like profiles (Fig. 6B and D, arrows). An abnormal fragmentation of the Golgi apparatus (Fig. 6D) with dilatation of cisterns (Fig. 6B and D) was also often observed, as inferred from the CTR433-immunostained sections displaying a clearly disorganized Purkinje cell Golgi complex (Supplementary Fig. 3), and in agreement with our previously reported electron microscopic study on *Yif1b*-KO CA1-hippocampal neurons (Alterio *et al.*, 2015). Morphological alterations were present in the Purkinje cell dendrites of mutant mice, such as large autophagosome-like vacuoles (Fig. 6F, arrowheads). In addition, consistent with the presence of some Golgian outpost-like profiles in the molecular layer (Supplementary Fig. 3, arrowheads), stacks of Golgi cisterns were often seen in primary dendritic profiles of *Yif1b*-KO Purkinje cells (Supplementary Fig. 4). Considering that Purkinje cell dendrites have been shown to have no Golgi outposts (Liu *et al.*, 2017), Golgi apparatus were abnormally targeted to dendrites in mutant Purkinje cells. The ER displayed the most diverse and notable aberrant configurations in *Yif1b*-KO Purkinje cells, such as unusual elongated loose network of rough ER (RER) cisterns throughout the peripheral cytoplasm and with less ordered arrays of RER in the perinuclear cytoplasm (Fig. 6B). Frequently, abnormal wavy segments of smooth ER (SER) were continuous with normal RER. Among alterations detected, RER cisterns were associated with clusters of abnormal dilated and very clear vesicles dispersed throughout the perinuclear cytoplasm, between RER cisterns and the nuclear envelope (Fig. 7A, arrows). Normal RER cisterns sometimes were continuous with abnormal and compacted aggregates of SER membranes which appeared as bulky stacks of ER cisterns attached to the neuronal membrane (Fig. 7B), sometimes with round and compacted agglomerates of SER membranes (Fig. 7C) or with concentric and compacted whorls of SER membranes (Fig. 7D). Such abnormal configurations of ER aggregates were constantly located in the basal pole near the emergence of the Purkinje cell axon (Supplementary Fig. 5).

Consistent with the reduced number of Purkinje cells identified with calbindin-immunostaining in *Yif1b*-KO mice sections, scattered or groups of Purkinje cell perikarya and dendrites in the molecular layer displayed ultrastructural features of advanced degeneration. Degenerating Purkinje cells appeared shrunken with numerous dilated Golgi cisterns, abnormal darkening of highly condensed cytoplasm and nucleoplasm surrounded by swollen profiles of the Bergmann glia (Fig. 7E). Ultrastructural features of apoptotic cell death, such as chromatin condensation and nuclear fragmentation (Dusart *et al.*, 2006) were not observed in our study, suggesting that Purkinje cells lacking *Yif1b* die by necrotic mechanisms. Consistent with this ultrastructural finding, no difference was observed in detection of apoptosis (Supplementary material) between wild-type and *Yif1b*-KO mice (Supplementary Fig. 6).

It should be noted that evident signs of alterations of Golgi apparatus and ER were observed in other neuronal types, such as in pyramidal neurons of the CA1-hippocampal layer (Alterio *et al.*, 2015; and Supplementary Fig. 7) and that these alterations did not impair the physiological properties of neurons, such as

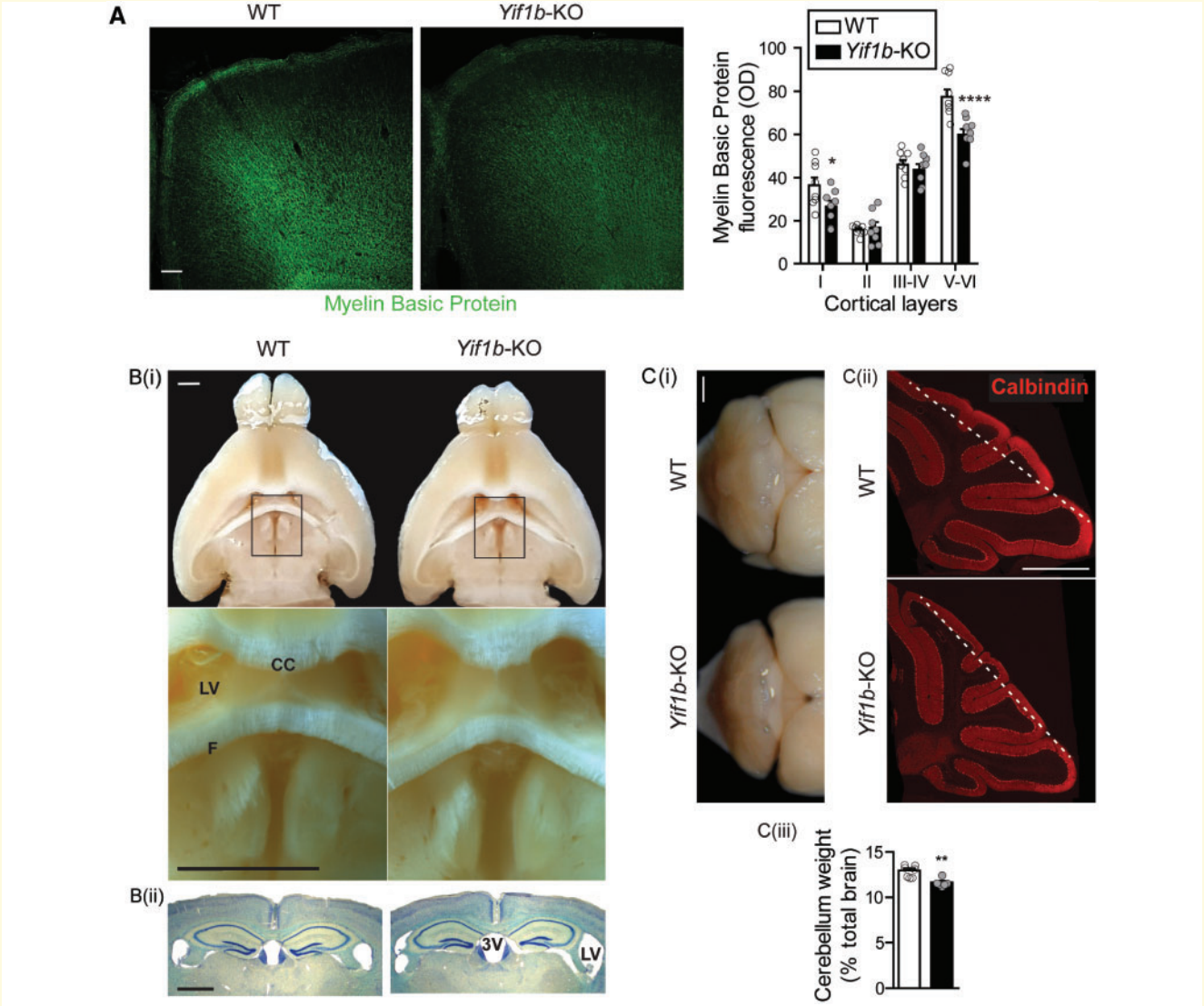

Figure 4 Histological and anatomical defects in *Yif1b*-KO brain. (**A**) In the motor cortex, MBP immunostaining revealed a decrease of myelination in *Yif1b*-KO compared to wild-type in layer I and layers V-VI [interaction layer × genotype, $F(3,42) = 7.422$, $P = 0.004$; $P < 0.05$ and $P < 0.0001$ in layer I and V-VI, respectively, wild-type versus *Yif1b*-KO with Bonferroni]. (**B**) Anatomical comparison of wild-type and *Yif1b*-KO mice brain shows the moderate enlargement of ventricles in *Yif1b*-KO compared to wild-type mice (enlargements of *insets* are *below*) on horizontal brain slices from 10-month-old mice [**B(i)**] and in Luxol fast blue-stained coronal sections [**B(ii)**]. (**C**) Cerebellar gross anatomy and histological sections, cerebellum related-behaviour in wild-type and *Yif1b*-KO. [**C(i)**] An upper view of the cerebellum shows reduction in size of *Yif1b*-KO compared to wild-type mice. [**C(ii)**] Change in the shape of cerebellar vermis revealed by Calbindin immunolabelling on parasagittal brain sections. [**C(iii)**] Quantification of cerebellum weight shows a decrease in *Yif1b*-KO ($n = 6$) as compared to wild-type ($n = 7$) (Mann-Whitney test, $P = 0.0082$). Data are presented as mean ± SEM and data-points are shown. $^{**}P < 0.01$, $^{****}P < 0.0001$. 3V = third ventricle; cc = corpus callosum; F = fornix; LV = lateral ventricle. Scale bars = 100 μm for **A**, 1 mm for **B(i)** and **C(ii)**, 500 μm for **B(ii)** and **C(i)**.

demonstrated by recordings in hippocampal neurons and remaining Purkinje cells (Supplementary material and Supplementary Fig. 8).

Yif1b/*YIF1B* deletion affects the primary cilium

Breeding *Yif1b*-KO male mice led us to uncover their infertility because of the lack of progeny of homozygous male *Yif1b*-KO mice (Supplementary Fig. 9A) and the quasi-absence of spermatozoa in their epididymis (Supplementary material and Supplementary Fig. 9B). The few remaining spermatozoa exhibited structural alterations of the flagella with disorganization of microtubule doublets or supernumerary flagella (Supplementary Fig. 9C). Altogether, cerebellar alteration, male sterility, visual and olfactory deficits (Supplementary material and Supplementary Fig. 10) in *Yif1b*-KO mice resemble some of the phenotypes observed

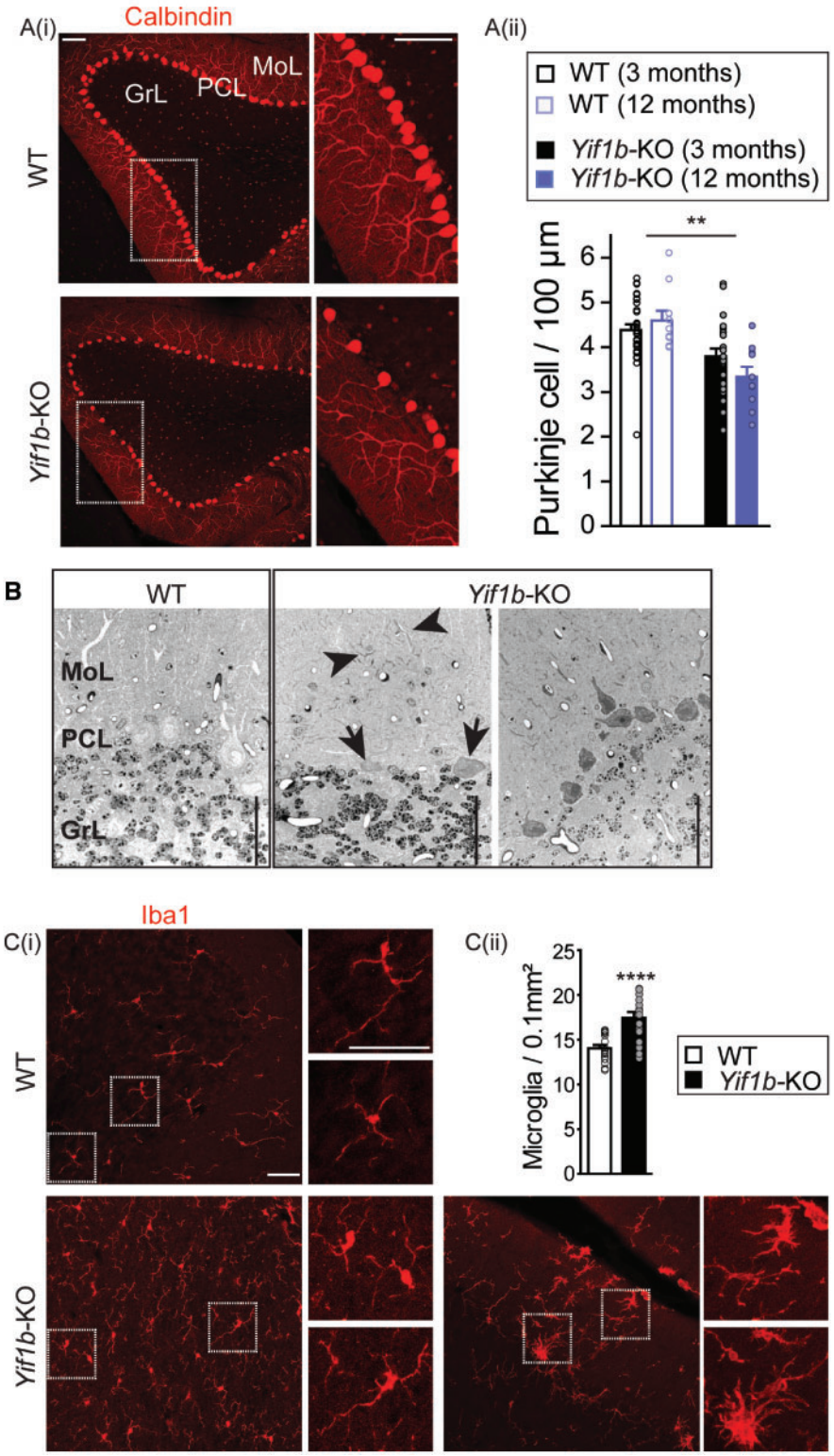

Figure 5 Cellular alterations in the cerebellum of *Yif1b*-KO mice. (**A**) Calbindin immunolabelling revealed fewer Purkinje cells in *Yif1b*-KO cerebellum compared to wild-type as shown on representative [**A(i)** 3-month-old mice] and quantified images [**A(ii)** wild-type, $n = 30$; *Yif1b*-KO, $n = 25$ from six and five animals, respectively, for 3-month-old animals, white and black bars; and wild-type, $n = 10$; *Yif1b*-KO, $n = 10$ from two animals of each genotype for 12-month-old animal, blue bars]. A two-way ANOVA indicated significant difference between genotypes [$F(1,71) = 20.8$, $P < 0.0001$] with no significant difference between age [$F(1,71) = 0.35$, $P = 0.555$] or genotype × age interaction [$F(1,71) = 2.69$, $P = 0.01055$]. Moreover, altered dendritic arborizations of Purkinje cells was observed in *Yif1b*-KO compared to wild-type (see enlarged images). (**B**) Semi-thin parasagittal resin sections (1–2 µm) stained with toluidine blue from the cerebellar cortex in the region of vermis including lobules IX and X. The cerebellar cortical layers in wild-type mice exhibit a normal cyto-architecture with somata of Purkinje cells containing a large pale

(continued)

in ciliopathies. Cilium integrity strongly relies on traffic from the Golgi apparatus, and YIF1B is essential for proper anterograde traffic and Golgi apparatus integrity (Alterio *et al.*, 2015). We thus investigated possible alterations of primary cilia in *Yif1b*-KO mice brains, focusing on the Purkinje cells layer of the cerebellum that was strongly affected in the mutant (Fig. 8). The immunolabelling for Arl13B [Fig. 8A(i)] demonstrated that the lack of *Yif1b* induced an increase in the length of primary cilia [Fig. 8A(ii)]. The axoneme of primary cilium in Purkinje cells is short (Del Cerro and Snider, 1969) and was very rarely observed in our electron microscopy analysis of the cerebellar cortex. To characterize the ultrastructural defects of the primary cilium and ciliary related structures, we examined pyramidal cells in the hippocampus that displays numerous long primary cilia (Wang *et al.*, 2011). We found in pyramidal neurons from CA1, alterations of structures involved in primary cilium anchorage, such as an increase in striated rootlet thickness extending from basal bodies and centrioles [Fig. 8B(i)], an increase in the inter-basal body/centriole distance and a reduction in the length of basal bodies [Fig. 8B(ii and iii)]. We then investigated the consequences of *YIF1B*/*Yif1b* deletion in primary cilia and basal body structures, in cultured fibroblasts of patients and mutant mice. Abundance of ciliated cells was significantly reduced in Patient 2.1 as compared to controls [Fig. 8C(i)]. Moreover, the average length of cilia, based on either acetylated tubulin [Fig. 8C(ii)] or Arl13B stainings was one-third shorter in Patients 2.1, 4.2 and 5.1 fibroblasts compared to controls [Fig. 8C(iii and v)]. These patients are carrying truncating mutations that lead to undetectable levels of YIF1B (Patients 2.1 and 5.1) or a point mutation leading to a highly reduced expression of YIF1B (Patient 4.2). Rootletin volume was increased in patient cells (Fig. 8C(iv and v)], suggesting changes in the rootlets that anchor primary cilia. However, CEP83 (Failler *et al.*, 2014) and CEP164 (Schmidt *et al.*, 2012) (components of the centriole and of distal appendages) immunostainings showed no change in basal body proteins [Fig. 8C(vi and vii)]. Consistently, cilia of *Yif1b*-KO mouse cultured skin fibroblasts were shorter than controls (Fig. 8D).

Discussion

Our work has unveiled 10 individuals from six independent families with recessive mutations in the *YIF1B* gene. These patients displayed some variability in their clinical features, however common phenotypic profile including severe global developmental and motor delay, central hypoventilation, seizures, visual alterations and brain abnormalities were observed with mutations leading to a truncated protein or a point-mutated *YIF1B* protein. Recently, a case report also identified patients carrying mutations in the *YIF1B* gene (AlMuhaizea *et al.*, 2020). Interestingly, one patient of 7 years of age (Family 5 of the case report) had a mutation similar to the patients of Family 1 from our study and was from the same Somalian origin. However, although the clinical features are similar, the patients identified in our study deceased at 15 months. This discrepancy between the effect of *YIF1B* mutation on survival, points out that lacking YIF1B has fatal consequences in human for the ability of feeding and the development of epilepsy. The patient with the p.Glu200* mutation (Family 5 of the case report published by AlMuhaizea *et al.*, 2020) is still alive but is fed by tube and their epilepsy is pharmacologically controlled. Remarkably, two children from the same family died at 2 months and 6 months, the latter from pneumonia, and had hypotonia similar to our Family 1 siblings. Comparing cases of the two studies clearly demonstrated that mutations in the *YIF1B* gene presumably leading to the absence of YIF1B protein are not always developing epilepsy. This is even more prone by the fact that the same mutation led to epilepsy in one patient, whereas her sister is not affected (Family 3 of the current study).

In this study, we demonstrated that truncation of the YIF1B protein after the first transmembrane domain led to undetectable levels of protein. This suggests that truncated YIF1B protein was instable or degraded, as previously observed when we attempted to express truncated YIF1B proteins in COS cells (Al Awabdh *et al.*, 2012). Furthermore, a point mutation in YIF1B protein led to a strong decrease of its expression (Patient 5.1). Thus, we can postulate that the loss of function of YIF1B is responsible for defects observed in patients. In this context, *Yif1b*-KO mice that constitutively lack YIF1B were analysed and we demonstrated that deletion of the *Yif1b* gene in adult mice recapitulated some defects observed in children carrying *YIF1B* mutations, such as enlargement of ventricle size, cerebellar dystrophy, locomotor alterations and visual deficits.

The clinical features of patients carrying *YIF1B* mutations did not fit with any previously described pathologies. However, some traits, such as severe neurodevelopmental

Figure 5 Continued

nucleus surrounded by a slightly stained pericaryon and unstained dendritic profiles in the molecular layer, whereas the cerebellar cortex of *Yif1b*-KO mice shows two Purkinje cells with moderately dense cell bodies (arrow) and darkening of proximal and distal dendritic processes (arrowhead) or grouped darkened Purkinje cells, suggesting different stages of degeneration. (**C**) Increased microglial activation revealed by density of microglia throughout the cerebellar cortex and foci of Iba1-positive cells [**C(i)**, representative images; **(ii)**, quantification (wild-type, $n = 16$; *Yif1b*-KO, $n = 16$; Student's *t*-test, $P < 0.0001$)]. Note the hypertrophic cell bodies and shortened thick processes in the molecular and Purkinje cells layers. Data are presented as mean ± SEM and data-points are shown. $^{**}P < 0.01$, $^{****}P < 0.0001$. GrL = granular cell layer; MoL = molecular layer; PCL = Purkinje cell layer. Scale bars = 100 μm for **A**, 50 μm for **B** and **C**.

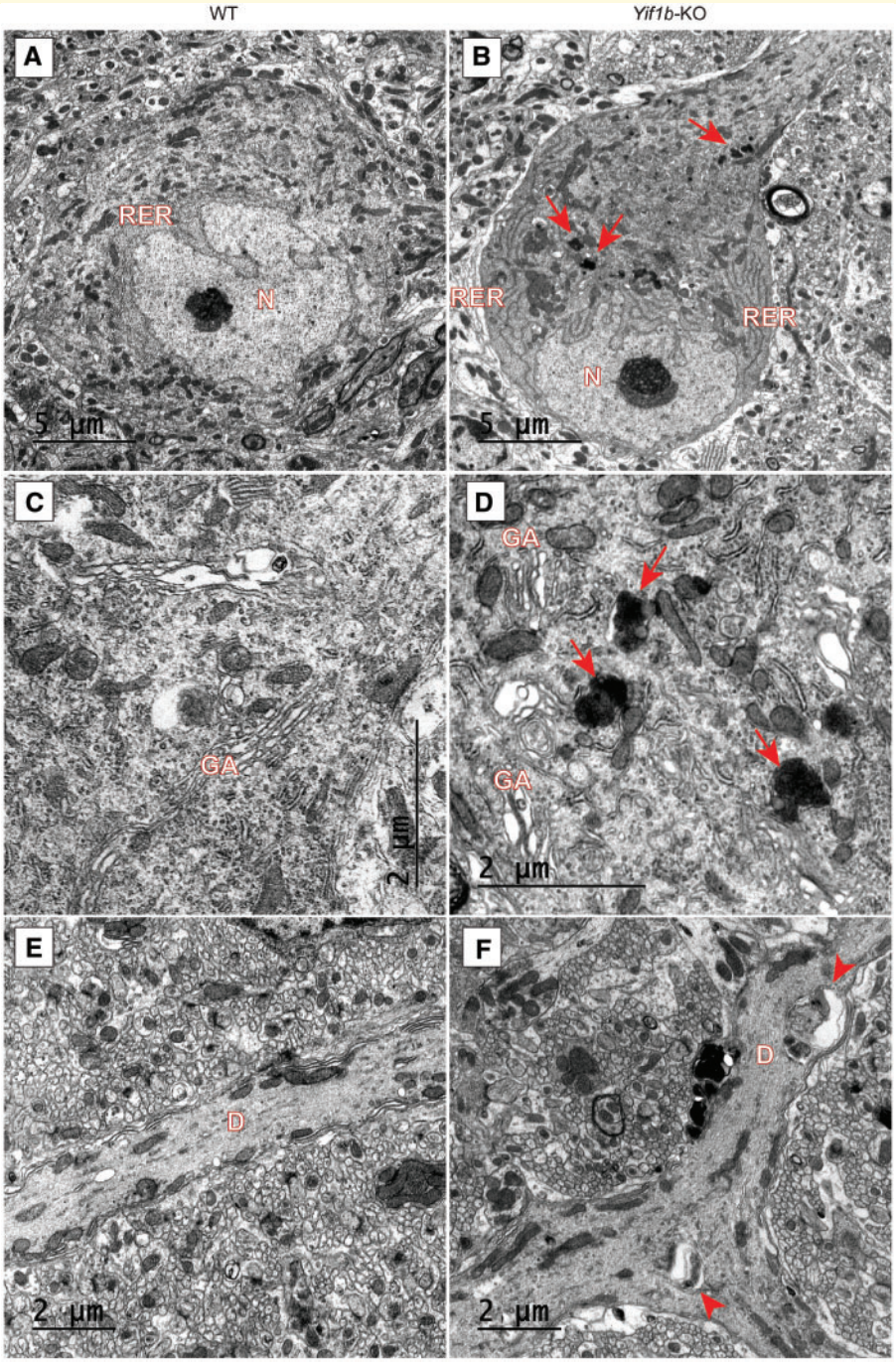

Figure 6 Transmission electron micrographs of Purkinje cells in the cerebellar cortex of wild-type and *Yif1b*-KO adult mice. (**A**, **C** and **E**) Representative ultrastructure of cerebellar Purkinje cells in wild-type mice. Micrograph illustrating the normal arrangement of the cytoplasmic organelles centred on the wrinkled nucleus and the regular array of the rough ER cisterns in the perinuclear zone (**A**). The typical ultrastructural aspect of the Purkinje cell Golgi complex organized as a compact stack of flat and long cisterns (**C**). A representative Purkinje cell dendritic process in the molecular layer showing a normal ultrastructure (**E**). (**B**, **D** and **F**) Ultrastructure of the Purkinje cells in the *Yif1b*-KO mice displaying morphological alterations in the perikaryon and the dendritic processes. The soma of a Purkinje cells exhibiting irregular arrangement of elongated and anastomosed cisterns of RER, largely dispersed throughout the perikaryon and the perinuclear zone (**B**). Note also the presence of lysosomes (arrows) scattered all over the perikaryon (**B** and **D**). Multiple short stacks of Purkinje cells Golgi complexes displaying abnormal dilated saccules (**D**). A Purkinje cells dendritic profile with two large autophagosome-like vacuoles (arrowheads) which are partially filled with masses of cytoplasmic material in a process of degradation (**F**). D = dendrite; GA = Golgi apparatus; N = nucleus; RER = rough endoplasmic reticulum.

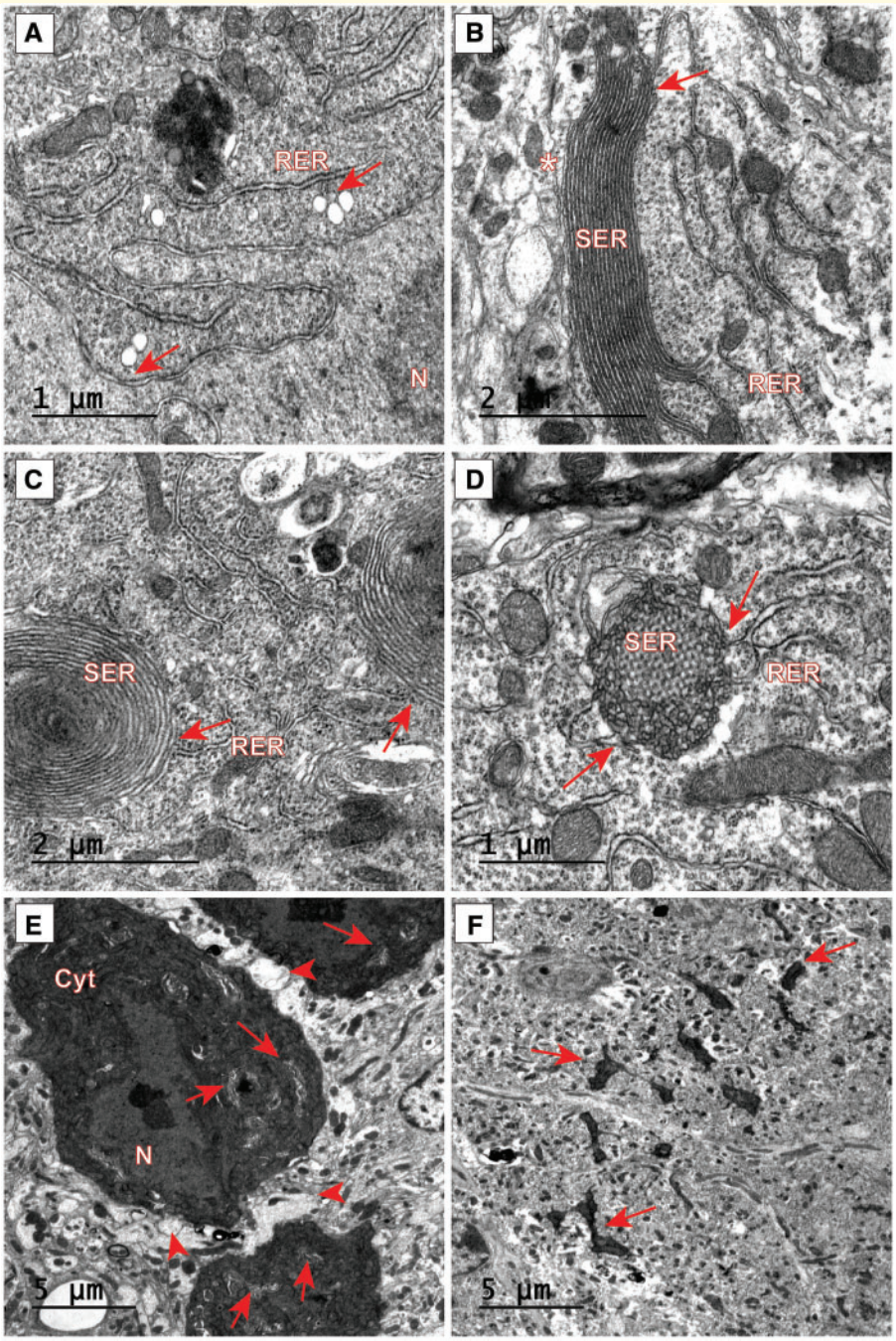

Figure 7 Electron micrographs showing diverse RER ultrastructural abnormalities and degenerating dark Purkinje cells in *Yif1b*-KO adult mice. (**A**) Abnormal clusters composed of two to three enlarged vesicles with a transparent lumen which appear systematically associated with RER cisterns (arrows) and very close to the nuclear envelope. (**B**) Abnormal compact and thick stack of parallel ER cisterns with the lumen almost entirely obliterated and connected with normal cisterns of RER (arrows). The aberrant stack is located at the periphery of the Purkinje cells and closely apposed to the cell membrane (asterisk). (**C**) The ultrastructure of a Purkinje cells displaying two moderately compacted ER whorls of RER cisterns (arrows). (**D**) Abnormal round ER agglomerate displaying a central crystalline arrangement of tubules. Note on their periphery the continuity with RER cisterns (arrows). (**E** and **F**) Electron micrographs at low magnification of some degenerating darkened Purkinje cells. The darkened cell bodies have an irregular pyknotic nucleus with homogenous nucleoplasm without obvious heterochromatin. The cytoplasm is dense with the organelles tightly packed and displaying accumulations of intensely stained ER membranes and dilated Golgi complexes scattered throughout the cytoplasm (arrows). Degenerating neurons are covered with enlarged clear astroglial profiles (arrowhead) with rare basket synapses (**E**). Moderate darkened shrunken Purkinje cells dendritic profiles in molecular layer (**F**, arrows). Scale bars are represented on the pictures. Cyt = cytoplasm; N = nucleus; RER = rough ER; SER = smooth ER.

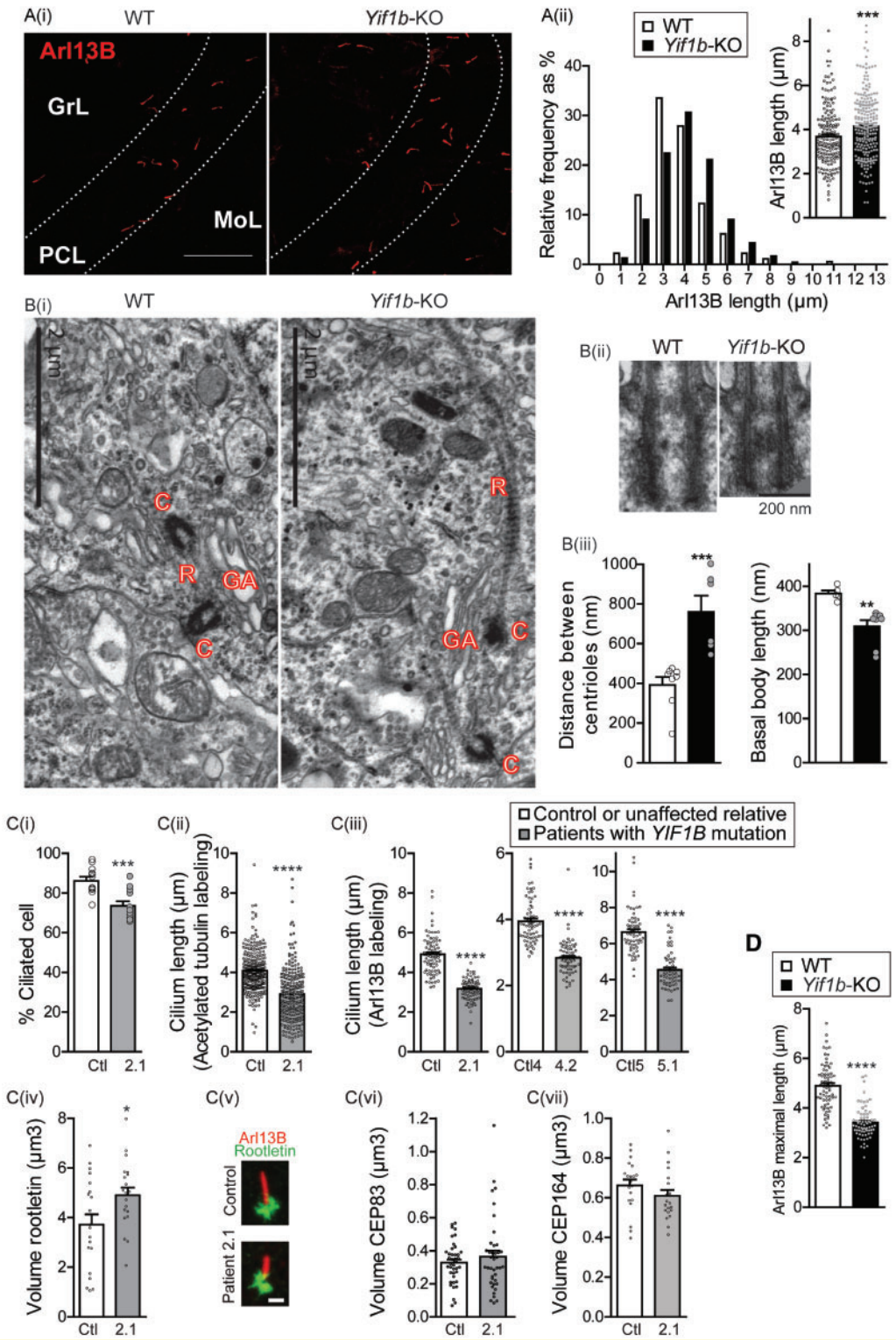

Figure 8 Impact of the loss of *Yif1b*/*YIF1B* on the primary cilium. (**A**) Primary cilia in cerebellum sections of wild-type and *Yif1b*-KO mice. [**A(i)**] Cerebellar sections immunolabeled with Arl13B, a ciliary marker. [**A(ii)**] Distribution of cilium length and ciliary length means were quantified in Purkinje cell layer of cerebellar lobules 9 and 10 respectively (wild-type, $n = 185$ and *Yif1b*-KO, $n = 269$ cilium, eight images of four animals per genotype). Cilia were significantly longer in *Yif1b*-KO compared to wild-type (11.4% increase of mean; Mann-Whitney test, $P = 0.0005$). (**B**) Ultrastructural analysis of CA1 pyramidal neurons of *Yif1b*-KO mice revealed alterations in primary cilia. Representative pictures showing close interaction of Golgi apparatus with rootlets and centrioles [**B(i)**], and the basal body ultrastructural morphology [**B(ii)**]. Quantification of the distance between centrioles (wild-type, $n = 8$; *Yif1b*-KO, $n = 6$; Mann-Whitney, $P = 0.0007$) and of the basal body length in wild-type and *Yif1b*-KO neurons (wild-type, $n = 5$; *Yif1b*-KO, $n = 8$; Mann-Whitney, $P = 0.0042$) [**B(iii)**]. (**C**) Quantification of cilium components in cultured fibroblasts from control and patients' skin. Percentage of ciliated cells (control, $n = 13$ fields, 337 cells; Patient 2.1, $n = 12$ fields, 332

(continued)

delay, white matter defects and/or progressive cerebral atrophy and intellectual disability were similar to a class of illnesses recently classified as Golgipathies (Passemard *et al.*, 2017). YIF1B is a trafficking protein that interacts with the small GTPase Rab6 and Yip1A, another trafficking protein (Al Awabdh *et al.*, 2012). Golgipathies include diseases in which mutated genes encoded Golgi apparatus proteins but also vesicular carriers involved in the sorting, packing, routing and recycling through interactions with Rab GTPases, Rab effectors or Rab regulators that orchestrate secretory pathways. Here, we also demonstrated that *Yif1b* deletion leads to disorganization of the ER in mice hippocampal neurons and cerebellar Purkinje cells. Such alteration was also visualized after complete depletion of YIP1A expression (Dykstra *et al.*, 2010), a protein directly interacting with YIF1B (Al Awabdh *et al.*, 2012). ER and Golgi apparatus disorganized morphologies has been also observed when the ER resident protein BCAP31 is mutated in patients and is associated with motor and intellectual disabilities, dystonia, cerebellar atrophy and poor myelination (Cacciagli *et al.*, 2013).

We previously showed that YIF1B is involved in the anterograde traffic from ER to the cell membrane and more particularly to specific subcompartments of the neuronal cellular membrane, but also in Golgi apparatus morphology (Carrel *et al.*, 2008; Al Awabdh *et al.*, 2012; Alterio *et al.*, 2015). In this study, we demonstrate that at the cellular level, YIF1B is also essential for ER morphology and primary cilium integrity and that its deletion leads to alteration of the myelination and to neuronal death. We will discuss how cellular alterations observed in the CNS of the *Yif1b*-KO mutant mice could participate to brain alterations observed in patients carrying *YIF1B* mutations.

Myelination in the brain relies on proliferation, migration and differentiation of oligodendrocyte progenitor cells in mature oligodendrocytes that are able to synthesize myelin sheaths to insulate axons. On one hand, the myelin protein plasmolipin (PLLP) assembles liquid-ordered lipids in the Golgi apparatus to allow their targeting to the cell membrane for generating new membranes necessary for myelination (Yaffe *et al.*, 2015), demonstrating the crucial role of Golgi apparatus in myelination. On the other hand, several receptors have been proposed to be implicated as regulators in oligodendrocyte maturation necessary for myelination (Mogha *et al.*, 2016). Alteration of anterograde traffic and Golgi apparatus disorganization (Alterio *et al.*, 2015) or mistargeting of specific receptors (Carrel *et al.*, 2008) in *Yif1b* depleted oligodendrocytes could be responsible for altered myelination.

Patients carrying *YIF1B* mutations presented progressive cerebellar atrophy and progressive parenchymal reduction. However, the cellular mechanisms that led to these defects could not be studied in brains from deceased patients since none was ever analyzed by anatomo-pathology. Among the mechanisms that lead to cerebellar atrophy during post-natal development in patients, the reduced number of Purkinje cells (like that observed in mutant mice) could be implicated. The cellular death could result from the defect of ER-Golgi apparatus transport. Indeed, it has been shown that inhibition of ER-Golgi apparatus traffic was linked to neurodegeneration in a pathological model, such as ALS (Soo *et al.*, 2015). On another hand, it has been demonstrated that the deletion of GM130, a Golgi apparatus protein, caused Golgi apparatus fragmentation, impaired secretory trafficking in Purkinje cells, and resulted in Purkinje cells cell death (Liu *et al.*, 2017), suggesting that Golgi apparatus disorganization could also be implicated in neuronal death. Golgi apparatus defects could also contribute to the progressive parenchymal reduction observed in the cortex of patients by altering dendritic organization. We recently demonstrated that the deletion of *Yif1b* in mice led to the decrease of the number of dendritic spines in the hippocampus (Martin *et al.*, 2020) and here, we found abnormal localization of Golgi apparatus in the initial segment of Purkinje cells dendrites in the cerebellum. Growing evidence indicates that the secretory pathway regulates dendritic growth and maintenance. Suppression of the ER-Golgi apparatus transport inhibits dendrite outgrowth in developing mammalian neurons (Horton *et al.*, 2005; Ye *et al.*, 2007) and deletion of GM130 in mice, which slows down the anterograde traffic, induces a reduction of dendritic size and arborization in the cerebellum (Liu *et al.*, 2017). Furthermore, in *Drosophila*, Yif1 plays a key role in the dendrite pruning in ddaC sensory neurons during early metamorphosis (Wang *et al.*, 2018). How accumulation of Golgi apparatus in the dendritic tree or the acceleration of the anterograde traffic could affect dendritic arborization, dendritogenesis and/or maintenance of dendritic spines should be further

Figure 8 Continued

cells; *t*-test with Welch's correction, $P < 0.0001$) [**C(i)**]. Cilium length using acetylated tubulin staining [**C(ii)**; control, $n = 284$, Patient 2.1, $n = 270$] and Arl13B staining [**C(iii)**; control ctl, ctl4 (unaffected sister), ctl5 (unaffected mother], $n = 70–80$; Patients 2.1, 3.1 and 5.1, $n = 70–80$; Student's *t*-test with Welch's correction or Mann-Whitney test, $P < 0.0001$]. Volume of rootletin [**C(iv)** controls, $n = 20$, Patient 2.1, $n = 20$; Student's *t*-test, $P = 0.0268$; **C(v)** representative pictures of Arl13B and rootletin immunostaining *below* graphs]. Volume of CEP83 [**C(vi)**] and CEP164 [**C(vii)**], identified by labelling adjacent to cilia (control, $n = 20$, Patient 2.1, $n = 20$). (**D**) The quantification of cilium length was performed using Arl13B staining on fibroblasts isolated from mice skin (wild-type, $n = 70$; *Yif1b*-KO, $n = 70$, Mann-Whitney test, $P < 0.0001$). Scale bars = 20 μm in **A**, and 2 μm in **B**. Data are presented as mean ± SEM and data-points are shown. $^{*}P < 0.05$, $^{**}P < 0.01$, $^{***}P < 0.0001$. Scale bar = 20 μm for **A(i)**. C = centriole; GA = Golgi apparatus; GrL = granular cell layer; MoL = molecular layer; PCL = Purkinje cell layer; R = rootlet.

investigated in *Yif1b*-KO mice. However, it suggests that these defects could account for the reduction of cerebral grey matter in patients carrying *YIF1B* mutations.

Golgi apparatus are involved in the delivery of cargo proteins to the primary cilium (Madhivanan and Aguilar, 2014; Stoetzel *et al.*, 2016), a tiny protrusion expressed at the surface of all cells which plays different functions depending on the developmental stage and the organ (Pampliega and Cuervo, 2016; Avalos *et al.*, 2017). Mechanistically, defects observed in primary cilia in the *Yif1b*-KO mouse could be a direct consequence of the Golgi apparatus alteration and/or abnormal trafficking from the Golgi apparatus to the cilium. This is supported by the disorganization of the Golgi apparatus in the mutant but also by previous results showing that the YIF1B protein is a chaperone protein for Rab-dependent trafficking along microtubules, a pathway that has been shown to be essential for protein sorting to the primary cilium and for ciliary length (Madhivanan and Aguilar, 2014). The more prominent effect of *Yif1b*/*YIF1B* deletion in mice and human is cerebellar atrophy. It has been demonstrated that Purkinje cells and Bergmann cells have cilia that were proposed to be involved in cerebellar development (Di Pietro *et al.*, 2017). Purkinje cells need intact ciliary Sonic Hedgehog (Shh) signalling for their proper development and dendritogenesis (Dahmane and Ruiz I Altaba, 1999; Cheng *et al.*, 2018). How primary cilium dysfunction in the cerebellum of *Yif1b*-KO mice affects this brain structure should be further explored, focusing on the kinetics of alterations of Purkinje cells and Bergman glia cell network in correlation with defects in Shh signalling. In addition, primary cilium alterations could also be implicated in visual deficit, male sterility and olfaction alterations observed in *Yif1b* depleted condition, as these defects are reminiscent of ciliopathies.

In summary, *YIF1B* is essential for post-natal brain maturation in human. Deletion of *Yif1b* in the mouse affects brain integrity with milder consequences than in human, suggesting that mice can overcome the lack of YIF1B during post-natal development. *Yif1b* deletion in mice induces cell-dependent subcellular alterations in the Golgi apparatus, the ER and the primary cilium/basal body structures that lead to an altered myelination and neuronal survival. Although the implication of the Golgi apparatus in primary cilium genesis has been evoked for a long time, our study demonstrates a link between Golgipathies and ciliopathies (Sorokin, 1962; Kim *et al.*, 2014). The crosstalk or cascade of events between Golgi apparatus and ER damage and ciliary defects, ultimately resulting in neurodevelopmental dysfunction remain to be clarified.

Acknowledgements

We thank the patients and their families for their participation, Alice Meunier for helpful discussions, Gilles Fortin and Sabine Levi for their expertise in ventilation and kindling, Axelle Simon and Sandra Autran for technical help and the UMS 28-NAC staff for technical assistance and animal care. The polyclonal rabbit antibody anti-Myelin Basic Protein is a generous gift from Dr D. R. Colman (Colman *et al.*, 1982). Confocal imaging was performed at the platform PICPEN from Centre de Psychiatrie et Neurosciences. Electron microscopy was performed at the Cellular and Molecular Imaging Platform, CRP2 – UMS 3612 CNRS—US25 Inserm-IRD—Université Paris Descartes.

Funding

This work was supported by grants from the Institut National de la Santé et de la Recherche Médicale (INSERM), Université Paris Descartes (ANR-11-IDEX-05-02), ANR-IHU and The Rare Diseases Foundation (France). J.M. is supported by Centre National de la Recherche Scientifique (CNRS). H.N. is supported by the Cognitive Science and Technology Council of Iran (grant number 1894).

Competing interests

The authors declare no competing financial interests.

Supplementary material

Supplementary material is available at *Brain* online.

References

Al Awabdh S, Miserey-Lenkei S, Bouceba T, Masson J, Kano F, Marinach-Patrice C, et al. A new vesicular scaffolding complex mediates the G-protein-coupled 5-HT1A receptor targeting to neuronal dendrites. J Neurosci 2012; 32: 14227–41.

AlMuhaizea M, AlMass R, AlHargan A, AlBader A, Medico Salsench E, Howaidi J, et al. Truncating mutations in YIF1B cause a progressive encephalopathy with various degrees of mixed movement disorder, microcephaly, and epilepsy. Acta Neuropathol 2020; 139: 791–4.

Alterio J, Masson J, Diaz J, Chachlaki K, Salman H, Areias J, et al. Yif1B is involved in the anterograde traffic pathway and the Golgi architecture. Traffic 2015; 16: 978–93.

Avalos Y, Pena-Oyarzun D, Budini M, Morselli E, Criollo A. New roles of the primary cilium in autophagy. Biomed Res Int 2017; 2017: 4367019.

Cacciagli P, Sutera-Sardo J, Borges-Correia A, Roux JC, Dorboz I, Desvignes JP, et al. Mutations in BCAP31 cause a severe X-linked phenotype with deafness, dystonia, and central hypomyelination and disorganize the Golgi apparatus. Am J Hum Genet 2013; 93: 579–86.

Carrel D, Masson J, Al Awabdh S, Capra CB, Lenkei Z, Hamon M, et al. Targeting of the 5-HT1A serotonin receptor to neuronal dendrites is mediated by Yif1B. J Neurosci 2008; 28: 8063–73.

Cheng FY, Fleming JT, Chiang C. Bergmann glial sonic hedgehog signaling activity is required for proper cerebellar cortical expansion and architecture. Dev Biol 2018; 440: 152–66.

Colman DR, Kreibich G, Frey AB, Sabatini DD. Synthesis and incorporation of myelin polypeptides into CNS myelin. J Cell Biol 1982; 95 (Pt 1): 598–608.

Cvetanovic M, Ingram M, Orr H, Opal P. Early activation of microglia and astrocytes in mouse models of spinocerebellar ataxia type 1. Neuroscience 2015; 289: 289–99.
Dahmane N, Ruiz I Altaba A. Sonic hedgehog regulates the growth and patterning of the cerebellum. Development 1999; 126: 3089–100.
Del Cerro MP, Snider RS. The Purkinje cell cilium. Anat Rec 1969; 165: 127–30.
Di Pietro C, Marazziti D, La Sala G, Abbaszadeh Z, Golini E, Matteoni R, et al. Primary cilia in the murine cerebellum and in mutant models of medulloblastoma. Cell Mol Neurobiol 2017; 37: 145–54.
Dusart I, Guenet JL, Sotelo C. Purkinje cell death: differences between developmental cell death and neurodegenerative death in mutant mice. Cerebellum 2006; 5: 163–73.
Dykstra KM, Pokusa JE, Suhan J, Lee TH. Yip1A structures the mammalian endoplasmic reticulum. Mol Biol Cell 2010; 21: 1556–68.
Failler M, Gee HY, Krug P, Joo K, Halbritter J, Belkacem L, et al. Mutations of CEP83 cause infantile nephronophthisis and intellectual disability. Am J Hum Genet 2014; 94: 905–14.
Feinstein M, Flusser H, Lerman-Sagie T, Ben-Zeev B, Lev D, Agamy O, et al. VPS53 mutations cause progressive cerebello-cerebral atrophy type 2 (PCCA2). J Med Genet 2014; 51: 303–8.
Handley MT, Morris-Rosendahl DJ, Brown S, Macdonald F, Hardy C, Bem D, et al. Mutation spectrum in RAB3GAP1, RAB3GAP2, and RAB18 and genotype-phenotype correlations in warburg micro syndrome and Martsolf syndrome. Hum Mutat 2013; 34: 686–96.
Horton AC, Racz B, Monson EE, Lin AL, Weinberg RJ, Ehlers MD. Polarized secretory trafficking directs cargo for asymmetric dendrite growth and morphogenesis. Neuron 2005; 48: 757–71.
Jasmin BJ, Cartaud J, Bornens M, Changeux JP. Golgi apparatus in chick skeletal muscle: changes in its distribution during end plate development and after denervation. Proc Natl Acad Sci USA 1989; 86: 7218–22.
Kim H, Xu H, Yao Q, Li W, Huang Q, Outeda P, et al. Ciliary membrane proteins traffic through the Golgi via a Rabep1/GGA1/Arl3-dependent mechanism. Nat Commun 2014; 5: 5482.
Liegel RP, Handley MT, Ronchetti A, Brown S, Langemeyer L, Linford A, et al. Loss-of-function mutations in TBC1D20 cause cataracts and male infertility in blind sterile mice and Warburg micro syndrome in humans. Am J Hum Genet 2013; 93: 1001–14.
Liu C, Mei M, Li Q, Roboti P, Pang Q, Ying Z, et al. Loss of the golgin GM130 causes Golgi disruption, Purkinje neuron loss, and ataxia in mice. Proc Natl Acad Sci USA 2017; 114: 346–51.
Madhivanan K, Aguilar RC. Ciliopathies: the trafficking connection. Traffic 2014; 15: 1031–56.
Martin V, Mathieu L, Diaz J, Salman H, Alterio J, Chevarin C, et al. Key role of the 5-HT1A receptor addressing protein Yif1B in serotonin neurotransmission and SSRI treatment. J Psychiatry Neurosci 2020; 45: 190134.
Matern H, Yang X, Andrulis E, Sternglanz R, Trepte HH, Gallwitz D. A novel Golgi membrane protein is part of a GTPase-binding protein complex involved in vesicle targeting. EMBO J 2000; 19: 4485–92.
Mir A, Kaufman L, Noor A, Motazacker MM, Jamil T, Azam M, et al. Identification of mutations in TRAPPC9, which encodes the NIK- and IKK-beta-binding protein, in nonsyndromic autosomal-recessive mental retardation. Am J Hum Genet 2009; 85: 909–15.
Mogha A, D'Rozario M, Monk KR. G protein-coupled receptors in myelinating glia. Trends Pharmacol Sci 2016; 37: 977–87.
Palay SL, Chan-Palay V. Cerebellar cortex: cytology and organization. Berlin, Heidelberg, New York: Springer; 1974.
Pampliega O, Cuervo AM. Autophagy and primary cilia: dual interplay. Curr Opin Cell Biol 2016; 39: 1–7.
Passemard S, Perez F, Colin-Lemesre E, Rasika S, Gressens P, El Ghouzzi V. Golgi trafficking defects in postnatal microcephaly: the evidence for 'Golgipathies'. Prog Neurobiol 2017; 153: 46–63.
Schmidt KN, Kuhns S, Neuner A, Hub B, Zentgraf H, Pereira G. Cep164 mediates vesicular docking to the mother centriole during early steps of ciliogenesis. J Cell Biol 2012; 199: 1083–101.
Seifert W, Kuhnisch J, Maritzen T, Horn D, Haucke V, Hennies HC. Cohen syndrome-associated protein, COH1, is a novel, giant Golgi matrix protein required for Golgi integrity. J Biol Chem 2011; 286: 37665–75.
Shamseldin HE, Bennett AH, Alfadhel M, Gupta V, Alkuraya FS. GOLGA2, encoding a master regulator of Golgi apparatus, is mutated in a patient with a neuromuscular disorder. Hum Genet 2016; 135: 245–51.
Sobreira N, Schiettecatte F, Valle D, Hamosh A. GeneMatcher: a matching tool for connecting investigators with an interest in the same gene. Hum Mutat 2015; 36: 928–30.
Soo KY, Halloran M, Sundaramoorthy V, Parakh S, Toth RP, Southam KA, et al. Rab1-dependent ER-Golgi transport dysfunction is a common pathogenic mechanism in SOD1, TDP-43 and FUS-associated ALS. Acta Neuropathol 2015; 130: 679–97.
Sorokin S. Centrioles and the formation of rudimentary cilia by fibroblasts and smooth muscle cells. J Cell Biol 1962; 15: 363–77.
Stoetzel C, Bar S, De Craene JO, Scheidecker S, Etard C, Chicher J, et al. A mutation in VPS15 (PIK3R4) causes a ciliopathy and affects IFT20 release from the cis-Golgi. Nat Commun 2016; 7: 13586.
Tay TL, Mai D, Dautzenberg J, Fernandez-Klett F, Lin G, S, et al. A new fate mapping system reveals context-dependent random or clonal expansion of microglia. Nat Neurosci 2017; 20: 793–803.
Wang Q, Wang Y, Yu F. Yif1 associates with Yip1 on Golgi and regulates dendrite pruning in sensory neurons during Drosophila metamorphosis. Development 2018; 145.
Wang Z, Phan T, Storm DR. The type 3 adenylyl cyclase is required for novel object learning and extinction of contextual memory: role of cAMP signaling in primary cilia. J Neurosci 2011; 31: 5557–61.
Yaffe Y, Hugger I, Yassaf IN, Shepshelovitch J, Sklan EH, Elkabetz Y, et al. The myelin proteolipid plasmolipin forms oligomers and induces liquid-ordered membranes in the Golgi complex. J Cell Sci 2015; 128: 2293–302.
Ye B, Zhang Y, Song W, Younger SH, Jan LY, Jan YN. Growing dendrites and axons differ in their reliance on the secretory pathway. Cell 2007; 130: 717–29.